



Chen, M., Zhang, B., Friedemann, S., Allegri, G., & Hallett, S. R. (2021). Effects of Ferromagnetic & Carbon-Fibre Z-Pins on the Magnetic Properties of Composites. *Composites Science and Technology*, 207, [108749].

<https://doi.org/10.1016/j.compscitech.2021.108749>

Peer reviewed version

License (if available):
CC BY-NC-ND

Link to published version (if available):
[10.1016/j.compscitech.2021.108749](https://doi.org/10.1016/j.compscitech.2021.108749)

[Link to publication record in Explore Bristol Research](#)
PDF-document

This is the author accepted manuscript (AAM). The final published version (version of record) is available online via Elsevier at <https://doi.org/10.1016/j.compscitech.2021.108749> . Please refer to any applicable terms of use of the publisher.

University of Bristol - Explore Bristol Research

General rights

This document is made available in accordance with publisher policies. Please cite only the published version using the reference above. Full terms of use are available:
<http://www.bristol.ac.uk/red/research-policy/pure/user-guides/ebr-terms/>

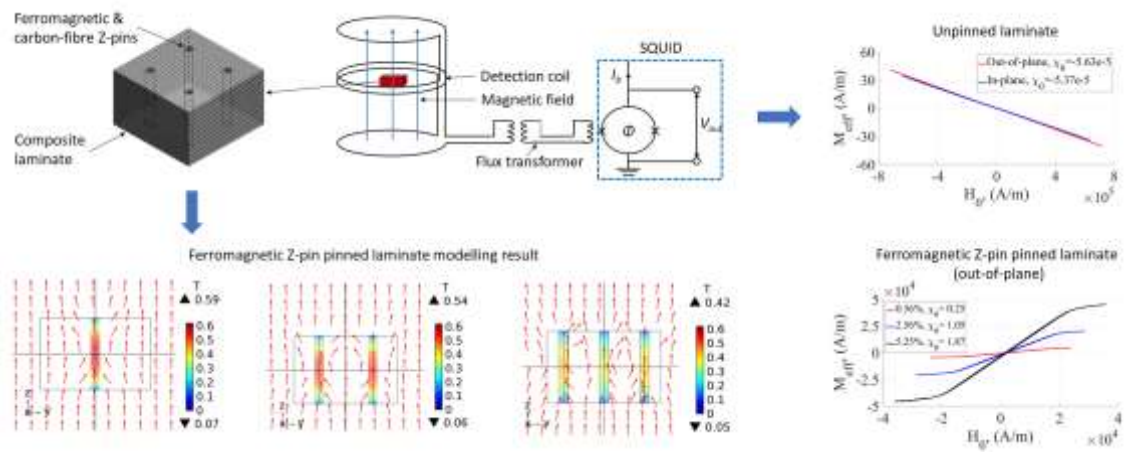
Effects of Ferromagnetic & Carbon-Fibre Z-Pins on the Magnetic Properties of Composites

Mudan Chen^a, Bing Zhang^{a,*}, Sven Friedemann^b, Giuliano Allegri^a, Stephen R. Hallett^a

^a *Bristol Composites Institute (ACCIS), University of Bristol, Bristol BS8 1TR, United Kingdom*

^b *HH Wills Laboratory, University of Bristol, Bristol BS8 1TL, United Kingdom*

Graphical Abstract



*Corresponding author email address: b.zhang@bristol.ac.uk (Bing Zhang)

Effects of Ferromagnetic & Carbon-Fibre Z-Pins on the Magnetic Properties of Composites

Mudan Chen^a, Bing Zhang^{a,*}, Sven Friedemann^b, Giuliano Allegri^a, Stephen R. Hallett^a

^a *Bristol Composites Institute (ACCIS), University of Bristol, Bristol BS8 1TR, United Kingdom*

^b *HH Wills Laboratory, University of Bristol, Bristol BS8 1TL, United Kingdom*

Abstract

This paper investigates for the first time the effects of Z-pins on the magnetic properties of composite laminates. In-plane and out-of-plane M-H curves of IM7/8552 laminates with and without Z-pins have been characterised by an MPMS3 SQUID magnetometer. Two kinds of pin materials (T300/BMI composite and ferromagnetic Ni/Fe alloy) have been studied at three different volume fractions (nominally 0.5%, 2% and 4%). The unpinned and carbon-fibre pinned laminates were found to be diamagnetic. The carbon-fibre pin had no significant influence on the global magnetic properties of the laminates. The Ni/Fe alloy pin increased the laminate linear-part magnetic volume susceptibility up to 1.87 and 0.13 for the out-of-plane and in-plane directions, respectively. Numerical modelling has been conducted to support the investigation of the effect of the pin volume fraction on the overall magnetic susceptibility and saturation magnetisation. The laminate out-of-plane susceptibility exhibits a nonlinear behaviour dependent on pin volume fraction, due to interactions between adjacent pins. The saturation magnetisation is proportional to the pin volume fraction and independent of field direction.

Keywords: A. Multifunctional composites, A. Laminate, B. Magnetic properties, C. Finite Element Analysis (FEA), Z-pin

1 **1 Introduction**

2 Fibre-reinforced plastic (FRP) laminates have outstanding in-plane performance,
3 but relatively weaker out-of-plane properties. Z-pinning has been developed as an
4 effective through-thickness reinforcement (TTR) technology [1], along with stitching
5 [2], tufting [3], 3D weaving [4], etc. A considerable amount of work has been reported
6 in the literature regarding the mechanical reinforcement function of Z-pins [5–11]. More
7 recently, there has been a strongly growing interest towards the exploration of multi-
8 functionality in composites, in addition to load bearing functions. A number of studies
9 have been published regarding the multi-functionality of Z-pinned composites [12–20].

10 Zhang et al. [12] characterised the Mode I & Mode II delamination self-sensing
11 function of Z-pinned laminates by measuring the real-time through-thickness electrical
12 resistance for both conductive and non-conductive fibre-reinforced plastics. They later
13 extended the delamination monitoring method to composites reinforced by conductive
14 Z-pin arrays and proposed a structural-level design strategy for multifunctional Z-
15 pinned composites [13]. The latter is based on connecting Z-pins both in series and in
16 parallel via arrays of electrodes attached to the laminate surface. Pegorin et al. [14]
17 experimentally evaluated the effects of pin material (carbon FRP and metals) and
18 volume content on the in-plane and through-thickness electrical conductivities at a
19 coupon scale. It was found that the through-thickness conductivity linearly increased
20 with pin volume content for all materials, and it was enhanced by a factor up to 10^6 by
21 copper Z-pins with a volume fraction of 1.84%. Pegorin et al. [15] also proposed a
22 Mode I delamination monitoring approach for laminates with Z-pin arrays. The
23 electrical resistance between top and bottom electrodes that were attached in unpinned
24 regions was found to increase with delamination length. Compared with unpinned

25 laminates, the resistance change of Z-pinned coupons due to delamination was much
26 larger, thus potentially enabling a versatile and robust monitoring of in-service damage.
27 Grigoriou et al. [16] later extended the electrical-based applications of Z-pins to
28 sandwich composites. In the research of Kadlec et al. [17], Z-pins were found to
29 effectively increase crack arrest ability of adhesive-bonded composite lap joints by 33%
30 under static load. At the same time, the electrical resistance across pins was observed to
31 have the same trend as crack growth, making this approach a promising candidate for
32 structural health monitoring, thus supporting the certification of adhesive-bonded joints
33 in aerospace applications.

34 By taking advantage of Z-pins combined with graphite sheets, Li et al. [18]
35 developed a structure with a 3D enhanced thermal conductivity. It was found that 2.7%
36 areal density of Z-pins enhanced the through-thickness and in-plane thermal
37 conductivities by 215% and 115%, respectively, compared with unpinned graphite sheet
38 composites. Through FE modelling, Pegorin et. al [19] found that the through-thickness
39 thermal properties of Z-pinned composites could be tailored via pin volume fraction and
40 the appropriate down-selection of pin materials, akin to the through-thickness electrical
41 properties. With the pins acting as the thermal pathways, the through-thickness thermal
42 conductivity grew linearly with pin content.

43 However, there is still a lack of studies regarding the effects of Z-pins on the
44 magnetic properties of composites. Traditional FRP composites are magnetically inert:
45 they do not show any remnant magnetism and only negligible enhancement of the
46 relative magnetic permeability [21]. The weaker magnetic properties of composites
47 compared to other materials represent an important limitation in several applications
48 (e.g. in electromagnetic machines) [22,23]. For instance, the rotor containment sleeves

49 of a permanent magnet machine are normally made of carbon/glass FRP composites or
50 weak-magnetic metals for load bearing. This generates a large non-magnetic gap
51 between the stator and the magnet, significantly reducing the resulting electromagnetic
52 force. Yon et al. [22] designed a magnetically semi-permeable sleeve to overcome this
53 drawback. Based on an analytical model, they estimated that an optimum relative
54 magnetic permeability ($\mu_r = 7.2$) could increase the fundamental component of the air-
55 gap flux density by 28%. A prototype machine with the sleeve made from cold-rolled
56 304L stainless steel ($\mu_r \approx 2$) was manufactured and tested. It showed a 20% increment of
57 the electromotive force compared to the magnetically inert material. However, the
58 stainless steel had a low resistivity and needed to be incorporated into a laminated
59 assembly, making the manufacture complex and expensive. With the same purpose,
60 Edwards et al. [23] incorporated magnetic particles into composites by employing
61 epoxy resin film loaded with pure iron particles into laminates. By embedding one film
62 between every adjacent ply (8 plies, 7 films), the predicted relative permeability was
63 improved, whilst the ultimate tensile strength was reduced to 60%.

64 Besides electromagnetic machines, Etches et al. [24] demonstrated how tailoring
65 the magnetic properties of composites can be potentially used for magnetic actuation of
66 the trailing edge of a morphing aerofoil. Two magnetic materials (barium ferrite and
67 ferrofluids) were separately embedded into hollow glass fibres. Due to the particle size
68 and viscosity, the maximum achievable volume fraction of barium ferrite was only 3%.
69 For ferrofluids, the filler volume fraction reached 30%. The ferrofluids-filled coupon
70 was successfully actuated in an applied magnetic field.

71 Compared with the methods for improving the magnetic properties of composites
72 reviewed above, Z-pinning offers a relatively wider material selection range, since Z-

73 pins can be in principle made of any material that can be processed into small rods.
74 Similar to the research on electrical and thermal properties of Z-pinned composites in
75 [12,14,18], this study also places emphasis on the effects of Z-pins on the global
76 physical properties of composites. Meanwhile, some local meso-scale analyses are also
77 presented to better understand the global effects observed. Specimen preparation and
78 experimental set-up are introduced in Section 2 and Section 3. The magnetic properties
79 of single Z-pins (not inserted into a composite laminate) are first characterised in
80 Section 4. Experimental results for Z-pinned laminate samples are then presented in
81 Section 5. The influence of pin misalignment and volume fraction on the magnetic
82 susceptibilities of through-thickness reinforced composites in both the in-plane and out-
83 of-plane directions are discussed in Section 6.

84 **2 Specimen preparation**

85 Metallic and carbon FRP Z-pins have been widely characterised for their
86 mechanical performance in the literature. 0.25 mm diameter Ni80/Fe20 permalloy pins
87 (from GoodFellow) and 0.28 mm diameter T300/BMI pins (from DPP BV) were
88 considered in this study.

89 Z-pinned laminate specimens were manufactured employing 16 plies of Hexcel's
90 IM7/8552 carbon/toughened-epoxy prepreg, with a stacking sequence of $[0^\circ/+45^\circ/90^\circ/-$
91 $45^\circ]_{2s}$. This quasi-isotropic (QI) stacking sequence is a representative configuration for
92 laminates in many structural applications. The maximum sample in-plane diagonal
93 length allowed was 4.8 mm, due to the configuration of the sample holder in the
94 MPMS3 magnetometer. Considering the pin spacing for nominal 0.5%, 2% and 4%
95 volume fractions, the Z-pinned coupons were designed to have the dimensions of

96 3.1×3.1 ×2 mm. Figure 1 (a) shows the configuration of a 2% pinned coupon as an
97 example.

98 The manufacturing process consisted of four steps. (1) The prepreg was defrosted
99 for 2 hours and laid up to form the laminate, with de-bulking after every four plies. (2)
100 The carbon-fibre pins were cut from a protruded rod stock and the alloy pins were cut
101 from a wire roll with scissors; then both types of Z-pins were manually inserted into the
102 uncured laminate. (3) The Z-pinned laminate was cured in an autoclave, following the
103 cycle recommended by Hexcel [25]. (4) Finally, the coupons were carefully cut from
104 the cured laminate using a water-cooled diamond-coated saw.

105 **3 Experimental set-up**

106 A SQUID (Superconducting Quantum Interference Device) magnetometer model
107 MPMS3 manufactured by Quantum Design was used in DC scan mode in this research
108 (Figure 1 (b)). The SQUID DC mode measures directly the magnetic flux of the sample
109 utilizing the Josephson effect, which employs interference of the wave function around
110 a superconducting loop where the magnetic flux of the sample is coupled in via a flux
111 transformer. Usage of gradiometer coils removes the signal from the applied magnetic
112 field, allowing to detect the magnetic flux from the sample as the sample is moved
113 through the gradiometer. From the measurement of the flux as a function of position in
114 the gradiometer, the magnetic moment of the sample is extracted using the MPMS3
115 software calibrated on a palladium standard [26,27]. A simplified schematic of the
116 measurement system is drawn in Figure 1 (c), with the SQUID highlighted in the dashed
117 green box, in which I_b is the bias current, Φ is the flux threading the SQUID, and V_{out} is
118 the voltage responding to the flux. The magnetic field in the MPMS3 is generated by a
119 superconducting electromagnet.

120 As shown in Figure 1 (b), the applied magnetic field was always in the vertical
121 direction. For the axial direction tests, a single z-pin (not inserted into the composite)
122 was glued on a quartz rod with a semicircle cross section and the pin axis was aligned
123 with the magnetic field direction. For the radial and angled pin tests, due to the pin
124 tending to align itself with the applied magnetic field, it was inserted into a fixed nylon
125 holder, to eliminate any rotation. The magnetic field was along the pin radius direction
126 for radial tests, and there was an angle between the magnetic field and pin axis for the
127 angled pin tests.

128 The Z-pinned laminate coupons were glued onto the nylon support cylinder and
129 put into a capsule. Nylon contributes a negligible background signal as its permeability
130 deviates less than 10^{-5} from that of free space [28], i.e. $1 < \mu_r < 1 + 10^{-5}$. The
131 magnetic field was applied along the 0° ply fibre direction (X axis) for the in-plane
132 measurements, whilst the magnetic field was along the specimen thickness direction (Z
133 axis) for the out-of-plane measurements.

134 In order to get a full M-H loop, the applied magnetic field H_0 was increased
135 linearly from zero to a field H_{\max} sufficient to observe magnetisation saturation, then
136 decreased to $-H_{\max}$, and finally brought back to H_{\max} . The total duration of one scan was
137 1.5 to 2 hours. Each scan was repeated twice to ensure the reliability of data.

138 **4 Single pin results**

139 In the experiments, the total magnetic moment of a sample was measured and
140 converted into an effective magnetisation using the measured sample volume. All the
141 M-H curves shown below present this effective magnetisation M_{eff} against the external
142 field H_0 . Note that the magnetisation is nonuniform inside the sample as we show later
143 in detail in the simulations. The effective magnetic susceptibility χ_0 of the tested

144 samples is extracted from linear fitting in the low-field regime of the M-H curve. From
145 this point, the low-field relative permeability is calculated as $\mu_r = \chi_0 + 1$.

146 **4.1 Carbon-fibre FRP pins**

147 In the DC SQUID option, a resolution of 10^{-9} A·m² is achieved by measuring a gel
148 capsule in a straw with the standard setup. For an individual carbon pin with its small
149 volume (diameter: $d = 0.28$ mm, length: $l = 4$ mm), however, the magnetic moment is
150 too small to be detected. This is consistent with the expected magnetic moment $m \approx$
151 7×10^{-11} A·m² in a field of $\mu_0 H_0 = 0.1$ T for a sample of this size containing pure
152 graphite [29] .

153 **4.2 Ni/Fe pins**

154 **4.2.1 Susceptibility vs. length**

155 Firstly, the effect of cure on the Ni/Fe Z-pin magnetic properties can be ignored,
156 which was confirmed by testing a pin before and after curing and observing that the
157 resulting M-H curves were the same.

158 The intrinsic magnetic permeability of Ni80/Fe20 permalloy is quite high [30],
159 however, in a finite size volume, the effects of demagnetisation give rise to a complex
160 variation of magnetisation M across the volume and hence the magnetic moment has a
161 non-linear dependence on magnetic field. In some limited cases, the demagnetizing
162 factor N can be used to obtain the internal field H as $H = H_0 - NM$. As reported
163 [31,32], the demagnetizing factor N of a cylinder is a complex function of the
164 susceptibility and ratio of length to diameter as well as the orientation of the magnetic
165 field. In small magnetic fields, a linear dependence can be approximated using the
166 demagnetizing factor N depending on the sample shape and orientation in magnetic
167 field only [33]. In this work the non-linear regime was also studied and finite element

168 analysis was used to model the behaviour of the samples, as analytical expressions are
169 not available.

170 Since the Ni/Fe pin has a constant diameter of 0.25 mm, pins with lengths ranging
171 from 1.5 to 4.1 mm in both the axial and radial directions were characterised. The
172 experimental single-pin M-H curves are plotted in Figure 2 (a, b). The slightly
173 horizontal offset of the M-H curves is most likely due to the remnant field in the
174 superconducting magnet following previous measurements at large magnetic fields.

175 For both directions, the magnetisation initially increases linearly with the applied
176 magnetic field H_0 , then, following a nonlinear response stage, it quickly reaches
177 saturation. The curves also reveal the very soft ferromagnetic behaviour of these
178 permalloy pins, as they have narrow hysteresis loops with very small coercive field and
179 remanence [30]. For the axial orientation, the slope of the low-field linear regime is
180 larger for longer samples and the non-linear response is shifted to lower fields for longer
181 samples, while the radial M-H behaviour is almost coincident for all samples. The
182 saturation magnetisation M_s is independent of pin length for both directions.

183 For a quantitative analysis, the low-field susceptibilities are plotted against the pin
184 length in Figure 2 (c, d). This shows that the susceptibility for axial field orientation
185 increases linearly from 21 to 100 with the pin length growing from 1.5 to 4.1 mm.
186 Conversely, the values for radial orientation of the field are much lower, having a mean
187 value of 2.5. In the low-field limit, the magnetic behaviour of the alloy pins can be
188 captured as that of a cylinder in an axial field with a demagnetizing factor, in agreement
189 with the linear M-H curve seen in the measurements at low fields. The demagnetizing
190 factor N_z decreases with the length to diameter ratio in agreement with the increased
191 effective susceptibility found in these measurements [31,32]. At the same time, the

192 demagnetizing factor N_x relating with the radially applied magnetic field is much higher
193 than N_z for a long thin cylinder [34] and relatively independent of the pin length, in
194 agreement with the experimental results.

195 **4.2.2 Susceptibility vs. inclination angle**

196 Since pin misalignment is a common and unavoidable manufacturing feature in Z-
197 pinned laminates, the effect of the inclination angle α (the angle between pin axis and
198 magnetic field) is explored. The out-of-plane misalignment angle usually varies
199 between 5° and 20° [35]. A 4.05 mm Ni/Fe pin was tested at pre-defined 0° , 20° , 40° ,
200 60° , 70° and 90° inclination angles with an accuracy of $\pm 2^\circ$.

201 The experimental M-H curves are plotted in Figure 3 (a). The curves show a
202 decrease of the initial slope and increase of the saturation field as the inclination angle
203 increases, whilst the saturation magnetisation remains independent on the angle. The
204 calculated saturation flux density B_s is around 1.1 T, which is consistent with the data
205 for 80% nickel permalloy from literature [30]. The low-field susceptibilities are
206 extracted and plotted in Figure 3 (b) as a function of the inclination angle. A nonlinear
207 decrease trend is observed as the inclination angle increases.

208 **5 Laminate results**

209 **5.1 Unpinned laminate**

210 The individual sample dimensions for the unpinned carbon fibre reinforced plastic
211 (CFRP) coupons were $3.2 \text{ mm} \times 3.1 \text{ mm} \times 2.0 \text{ mm}$. Since the laminate has a quasi-
212 isotropic stacking sequence, it is expected to exhibit negligible differences in magnetic
213 properties for any arbitrary in-plane direction.

214 The out-of-plane and in-plane M-H curves of the unpinned specimen are plotted in
215 Figure 4 (a). They present linear decreasing trends, and no saturation and hysteresis

216 were observed even at much higher H_{\max} values than those employed in the
217 characterisation of alloy Z-pins. This confirms that the CFRP considered here is a
218 weakly diamagnetic material [36]. The in-plane and out-of-plane M-H curves almost
219 coincide, with susceptibility values of -5.37×10^{-5} and -5.63×10^{-5} , respectively.

220 **5.2 Carbon-fibre Z-pin pinned laminate**

221 Three carbon-fibre Z-pin pinned coupons with different pin volume fractions were
222 tested. The actual volume fractions were calculated at 0.51%, 2.00% and 4.46%, by
223 accurately measuring the specimen dimensions and the pin length (including the small
224 amount of protruding top and bottom).

225 The in-plane and out-of-plane M-H curves are plotted in Figure 4 (b), with the
226 corresponding susceptibilities χ_0 listed in the legend. Similar to the case of the unpinned
227 CFRP, all curves present small monotonically decreasing trends, which implies that
228 carbon Z-pinned laminates are also diamagnetic in both in-plane and out-of-plane
229 directions. It appears that the absolute value of the susceptibility decreases with the pin
230 volume fraction for both directions. The out-of-plane susceptibility is quite close to that
231 of the in-plane direction. Compared with unpinned CFRP (i.e., comparing Figure 4 (a)
232 and (b)), the carbon fibre Z-pin reinforced coupons present effective susceptibilities
233 with the same order of magnitude as for unpinned CFRP. This proves that carbon fibre
234 pins have no large influence on the global magnetic susceptibility of a CFRP laminate.

235 **5.3 Ni/Fe Z-pin pinned laminate**

236 The actual pin volume fractions for the samples reinforced with alloy pins were
237 measured at 0.56%, 2.56% and 5.25%, respectively. The corresponding experimental
238 M-H curves are plotted in Figure 4 (c, d). The curves have similar trends to those for the
239 single Ni/Fe pin tests. The saturation magnetisation M_s increases with the pin volume

240 fraction for both in-plane and out-of-plane directions. Similar to the results on single
 241 alloy pins, M_s is independent from the field direction for a given pin volume fraction
 242 (i.e. comparing the same-colour curves in Figure 4 (c) and (d)).

243 As shown in the legends of Figure 4 (c, d), low-field effective susceptibilities in
 244 the linear response region for the 0.56%, 2.56%, 5.25% pinned samples are 0.25, 1.05,
 245 1.87 (out-of-plane) and 0.01, 0.07, 0.13 (in-plane), respectively. Compared with the
 246 diamagnetic unpinned coupon, the laminate with Ni/Fe Z-pins become strongly
 247 paramagnetic, with large susceptibilities. The low-field susceptibilities against pin
 248 volume fractions are plotted with solid lines in Figure 4 (e) and (f). For comparison, the
 249 dashed trend lines in Figure 4 (e) and (f) are given by the rule of mixtures:

$$250 \quad \chi_{0_sample} = (1 - V_{f_pin}) \cdot \chi_{0_lam} + V_{f_pin} \cdot \chi_{0_pin} \quad (1)$$

251 where χ_{0_sample} , χ_{0_lam} and χ_{0_pin} are the effective susceptibilities of pinned sample,
 252 unpinned laminate, and pin, respectively. V_{f_pin} is the pin volume fraction. Since χ_{0_lam}
 253 was measured to be very small for both directions (in the order of 10^{-5}), χ_{0_sample} is
 254 dominated by the pin volume fraction and susceptibility. When considering the in-plane
 255 behaviour, the experiments and analytical prediction agree well and only exhibit a slight
 256 difference for the 2.56% volume fraction sample. However, the difference is more
 257 evident for the out-of-plane direction especially at a higher pin volume fraction, which
 258 means that the magnetic susceptibility of the pinned samples does not increase linearly
 259 to the volume fraction of the soft-ferromagnetic through-thickness reinforcement. This
 260 is potentially due to the pin misalignment and interaction, which will be further
 261 investigated in the following section with the aid of finite element analysis (FEA).

262 **6 Discussion**

263 Comparing the test results for the unpinned laminate in Section 5.1 and the Ni/Fe
264 Z-pinned laminate in Section 5.3, it can be concluded that the magnetic properties of a
265 ferromagnetic pinned laminate are dominated by the pins. Since in Section 5.2 carbon-
266 fibre pins have been shown to have minor influence on the global magnetic behaviour of
267 composites, only the effects of Ni/Fe pins will be further discussed in this section,
268 considering the effects of pin misalignment, interaction, and volume fraction.

269 **6.1 Pin misalignment effect**

270 As illustrated in the experiments, the saturation magnetisation M_s is independent
271 of the inclination angle (Figure 3 (a)), and pin length (Figure 2 (a, b)). It has also been
272 demonstrated in Figure 4 (c) and (d) that M_s increases with pin volume fraction. Thus,
273 M_s will also increase with pin misalignment since the latter leads to a larger pin volume
274 fraction in a fixed thickness laminate with the pins running the full thickness.

275 The misalignment influences the low-field susceptibility of a Z-pinned laminate in
276 four aspects. Firstly, the effective susceptibility of the laminate will increase due to the
277 increased pin volume fraction caused by misalignment, similar to the saturation
278 magnetisation discussed above. Secondly, the longer pin length due to misalignment
279 will result in a change of the demagnetizing factor in a different way for in-plane and
280 out-of-plane orientations. The growth of pin length due to misalignment results in an
281 apparent increase of the effective susceptibility χ_0 of a single pin for the out-of-plane
282 direction (Figure 2 (c)), while no obvious influence for the in-plane property (Figure 2
283 (d)). Thirdly, the inclination angle due to pin misalignment has further effects on the
284 demagnetizing factor as shown in Figure 3 (b). For misalignment angle typically within
285 20° [35], it shows in Figure 3 (b) that the segment of 0° to 20° which corresponds to the

286 out-of-plane direction of Z-pinned laminate only slightly decreases, while the part from
 287 90°-70° related with the laminate in-plane direction has an apparent increment.
 288 Fourthly, pin misalignment would change the pin-to-pin distance in three dimensions
 289 and thus affect the pin interaction via magnetic field. A systematic study on the effect of
 290 pin misalignment will be addressed in a separate study by taking the aforementioned
 291 aspects into account.

292 **6.2 Pin volume fraction effect**

293 **6.2.1 Numerical modelling**

294 The commercial FEA tool COMSOL Multiphysics® was employed to help explain
 295 the influence of pin volume fraction. The magnetic vector potential \mathbf{A} is employed as a
 296 field variable for the element nodes in the FE models. The following equations are used
 297 for the magnetostatics case [37]:

$$298 \quad \nabla \cdot \mathbf{B} = 0 \quad (2)$$

$$299 \quad \mathbf{B} = \nabla \times \mathbf{A} \quad (3)$$

$$300 \quad \mathbf{B} = \mu_0(\mathbf{H} + \mathbf{M}) \quad (4)$$

301 where μ_0 is the vacuum permeability. The modelling strategy is verified through the
 302 alloy pin and pinned laminate tests as presented in Sections 4.2 and 5.3.

303 Each of the verification models consisted of the coupon (single pin or pinned
 304 laminate) in the middle of a relatively large free-space sphere and a layered infinite
 305 empty domain outside, as shown in Figure 5 by taking the 3 by 3 pin embedded
 306 laminate as an example. When modelling the tested Ni/Fe Z-pinned coupons, the pin
 307 misalignment must be considered since it affects the magnetic properties of composites
 308 as discussed in Section 6.1. To measure the pin misalignment, the sample top and
 309 bottom surfaces were scanned with a microscope, then each pin was located from the

310 scanned photos. Pin misalignment angles were determined by the distance between pin
311 ends and sample edges. For the 1-pinned, 4-pinned and 9-pinned samples, the average
312 misalignment angles are calculated as 9.1° , 8.4° , 6.3° respectively. Tetrahedral elements
313 were employed throughout the whole mesh. For all the models presented here, mesh
314 convergence studies have been conducted. There are 32 elements along the top or
315 bottom circle and 16 elements per/mm in the length direction. A uniform background
316 magnetic field was applied, which is consistent with the experimental set-up. The B-H
317 curve of 80% nickel permalloy (Figure 6) from the COMSOL nonlinear magnetic
318 material library [38] was used for the pin in the simulation. The material data in
319 COMSOL originates from the MagWeb database [39].

320 The modelling verification results are presented in the supplementary material. It
321 shows that good agreement between experimental measurements and modelling
322 predictions is obtained, and minor discrepancies only arise in the transition region for
323 60° and 70° angled pins. These differences could be attributed to the following factors.
324 Firstly, the pins are modelled as a cylinder, while the real pin end shape is not perfectly
325 flat after being cut with scissors. In addition, during the manufacturing process of wire
326 such as pull-out, the grain texture inside the wire might be changed, which might
327 influence the magnetic anisotropy and anisotropy of domain wall movements. Such
328 magnetic anisotropy was not taken into account in the modelling. However, the overall
329 simulation results are consistent with the experiments, especially for the most
330 interesting linear and plateau regions of the response. The FEA also allows observing
331 the flux density distribution inside pins, as shown in Figure 7 for the tested Ni/Fe Z-
332 pinned coupons.

333 **6.2.2 Model results discussion**

334 In order to study the volume fraction effect, three ideal coupons (all having 3.1
335 $\times 3.1 \times 2 \text{ mm}^3$ dimensions) respectively comprising 1, 4 and 9 pins were modelled with
336 all the pins perfectly straight, without protruding parts.

337 The linear-region susceptibility versus pin volume fraction curves of the three
338 models are plotted in Figure 8 (a, b). Similar with the experimental findings reported in
339 Figure 4 (e, f), the out-of-plane curves from the simulations present a clearly nonlinear
340 trend and it does not follow the rule of mixture in Figure 8 (a). On the other hand, the
341 rule of mixture gives good results for the in-plane curves, as seen in Figure 8 (b).

342 To understand this, the cross-section flux distribution given in Figure 9 must be
343 considered. For easy comparison, the colour bar ranges were set equal for each
344 direction, and the maximum and minimum flux values are listed beside the triangle
345 symbols in the graphs. For a single pin in the axial direction (out-of-plane), the flux is
346 maximal at the pin centre (Figure 9 (a)) due to the focusing of flux by the high
347 permeability of the material. In the radial direction, the flux is homogeneous over most
348 of the pin with a small increase at the ends (Figure 9 (d)).

349 For multiple pins, the flux density from the external field is distributed over
350 several pins and thus limits the enhancement of magnetisation compared to the case of a
351 single pin. Furthermore, the extent of this flux sharing increases with the pin volume
352 fraction and decreases with the pin spacing (comparing Figure 9 (b) and (c)). There are
353 no observable interactions between pins when the magnetic field is applied transversely,
354 and the flux density and distribution inside each pin show no significant dependence on
355 pin volume fraction.

356 The saturation magnetisation M_s as a function of pin volume fraction is plotted in
357 Figure 8 (c). This shows that the M_s is proportional to volume fraction for both
358 directions and independent from the magnetic field direction, as the in-plane and out-of-
359 plane curves completely coincide. This is simply because the pin volume fraction
360 determines the number of atomic magnetic moments per unit volume. The observation
361 also explains the experimental results for Ni/Fe pinned coupons reported in Section 5.3.

362 **7 Conclusions**

363 The magnetic properties of Z-pinned CFRP laminates have been investigated
364 experimentally and numerically. Several conclusions could be drawn here:

365 1) Carbon-fibre Z-pins do not have large influence on the global magnetic
366 properties of composites. 2) Soft ferromagnetic Ni/Fe Z-pins lead to a much larger
367 magnetic susceptibility in the axial direction than in the radial one. 3) Ni/Fe pins
368 enhance the laminate out-of-plane and in-plane low-field linear-region effective
369 susceptibilities up to 1.87 and 0.13 at 5.25% volume fraction, respectively. 4) The low-
370 field linear-region effective susceptibility of Ni/Fe pinned laminate increases with pin
371 volume fraction nonlinearly due to pin interactions for the out-of-plane direction, but
372 linearly for the in-plane orientation. 5) The global saturation magnetisation is only
373 dependent on pin volume fraction and independent from field direction.

374 In summary, it is feasible to tailor the magnetic properties of composites through
375 controlling the volume fraction of ferromagnetic pins. Embedding ferromagnetic
376 through-thickness reinforcement in FRP laminates can widen the application range of
377 FRP composites in electromagnetic applications.

378 **CRedit authorship contribution statement**

379 **Mudan Chen:** Methodology, Validation, Formal analysis, Investigation, Writing - Original Draft.

380 **Bing Zhang:** Conceptualization, Methodology, Validation, Formal analysis, Investigation, Resources,

381 Writing - Review & Editing, Supervision, Project administration. **Sven Friedemann**: Methodology,
382 Validation, Formal analysis, Investigation, Resources, Writing - Review & Editing, Supervision.
383 **Giuliano Allegri**: Conceptualization, Formal analysis, Writing - Review & Editing, Supervision.
384 **Stephen R. Hallett**: Conceptualization, Formal analysis, Resources, Writing - Review & Editing,
385 Supervision.

386 **Declaration of Competing Interest**

387 None

388 **Acknowledgements**

389 This work was supported by the Engineering and Physical Sciences Research
390 Council (EPSRC) through the Centre for Doctoral Training in Advanced Composites
391 for Innovation and Science (grant number EP/L016028/1). The COMSOL license was
392 supported by the Bristol University CAME School Pump-Priming fund 2019. We are
393 also grateful for advice given by Prof. Walther Schwarzacher and Dr Dmitry S. Ivanov
394 on data analysis, Dr Chrystel Remillat, Dr Kate Gongadze and Dr Robert Hughes on
395 simulations, as well as Mr Israel Osmond and Dr Mengze Zhu on experiments.

396 **References**

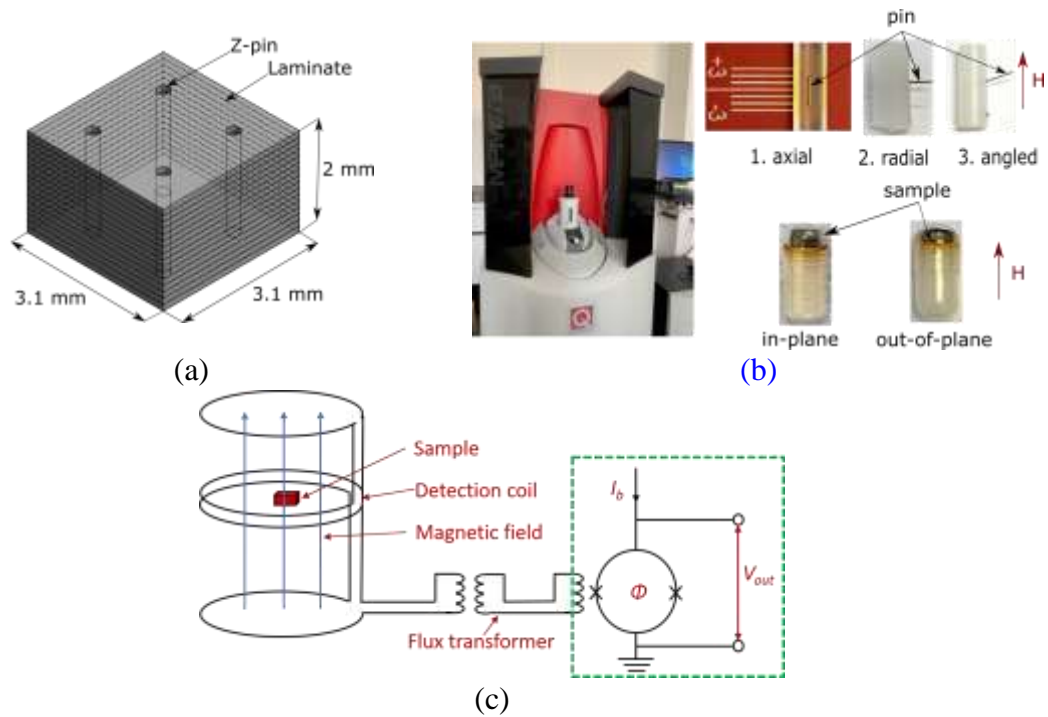
- 397 [1] A.P. Mouritz, Review of z-pinned laminates and sandwich composites,
398 *Composites Part A: Applied Science and Manufacturing*. 139 (2020) 106128.
399 <https://doi.org/10.1016/j.compositesa.2020.106128>.
- 400 [2] K. Dransfield, C. Baillie, Y.-W. Mai, Improving the delamination resistance of
401 CFRP by stitching—a review, *Composites Science and Technology*. 50 (1994)
402 305–317. [https://doi.org/10.1016/0266-3538\(94\)90019-1](https://doi.org/10.1016/0266-3538(94)90019-1).
- 403 [3] G. Dell’Anno, J.W.G. Treiber, I.K. Partridge, Manufacturing of composite parts
404 reinforced through-thickness by tufting, *Robotics and Computer-Integrated
405 Manufacturing*. 37 (2016) 262–272. <https://doi.org/10.1016/j.rcim.2015.04.004>.
- 406 [4] R. Gerlach, C.R. Siviour, J. Wiegand, N. Petrinic, In-plane and through-thickness
407 properties, failure modes, damage and delamination in 3D woven carbon fibre
408 composites subjected to impact loading, *Composites Science and Technology*. 72
409 (2012) 397–411. <https://doi.org/10.1016/j.compscitech.2011.11.032>.
- 410 [5] F. Warzok, G. Allegri, M. Gude, S.R. Hallett, Experimental study of Z-pin fatigue;
411 understanding of mode I and II coupon behaviour, *Composites Part A: Applied
412 Science and Manufacturing*. 127 (2019) 105615.
413 <https://doi.org/10.1016/j.compositesa.2019.105615>.

- 414 [6] A.R. Ravindran, R.B. Ladani, C.H. Wang, A.P. Mouritz, Hierarchical mode I and
415 mode II interlaminar toughening of Z-pinned composites using 1D and 2D carbon
416 nanofillers, *Composites Part A: Applied Science and Manufacturing*. 124 (2019)
417 105470. <https://doi.org/10.1016/j.compositesa.2019.05.038>.
- 418 [7] M. Li, P. Chen, B. Kong, T. Peng, Z. Yao, X. Qiu, Influences of thickness ratios of
419 flange and skin of composite T-joints on the reinforcement effect of Z-pin,
420 *Composites Part B: Engineering*. 97 (2016) 216–225.
421 <https://doi.org/10.1016/j.compositesb.2016.05.007>.
- 422 [8] F. Pegorin, K. Pingkarawat, S. Daynes, A.P. Mouritz, Influence of z-pin length on
423 the delamination fracture toughness and fatigue resistance of pinned composites,
424 *Composites Part B: Engineering*. 78 (2015) 298–307.
425 <https://doi.org/10.1016/j.compositesb.2015.03.093>.
- 426 [9] H. Cui, M. Yasaee, A.R. Melro, Dynamic inter-fibre failure of unidirectional
427 composite laminates with through-thickness reinforcement, *Composites Science
428 and Technology*. 176 (2019) 64–71.
429 <https://doi.org/10.1016/j.compscitech.2019.04.004>.
- 430 [10] B. M'membe, M. Yasaee, S.R. Hallett, I.K. Partridge, Effective use of metallic Z-
431 pins for composites' through-thickness reinforcement, *Composites Science and
432 Technology*. 175 (2019) 77–84.
433 <https://doi.org/10.1016/j.compscitech.2019.02.024>.
- 434 [11] J. Hoffmann, G. Scharr, Compression properties of composite laminates reinforced
435 with rectangular z-pins, *Composites Science and Technology*. 167 (2018) 463–
436 469. <https://doi.org/10.1016/j.compscitech.2018.08.042>.
- 437 [12] B. Zhang, G. Allegri, M. Yasaee, S.R.R. Hallett, I.K.K. Partridge, On the
438 delamination self-sensing function of Z-pinned composite laminates, *Composites
439 Science and Technology*. 128 (2016) 138–146.
440 <https://doi.org/10.1016/j.compscitech.2016.03.019>.
- 441 [13] B. Zhang, G. Allegri, S.R. Hallett, An experimental investigation into multi-
442 functional Z-pinned composite laminates, *Materials and Design*. 108 (2016) 679–
443 688. <https://doi.org/10.1016/j.matdes.2016.07.035>.
- 444 [14] F. Pegorin, K. Pingkarawat, A.P. Mouritz, Controlling the electrical conductivity
445 of fibre-polymer composites using z-pins, *Composites Science and Technology*.
446 150 (2017) 167–173. <https://doi.org/10.1016/j.compscitech.2017.07.018>.
- 447 [15] F. Pegorin, K. Pingkarawat, A.P. Mouritz, Electrical-based delamination crack
448 monitoring in composites using z-pins, *Composites Part A: Applied Science and
449 Manufacturing*. 104 (2018) 120–128.
450 <https://doi.org/10.1016/j.compositesa.2017.10.025>.
- 451 [16] K. Grigoriou, R.B. Ladani, A.P. Mouritz, Electrical properties of multifunctional
452 Z-pinned sandwich composites, *Composites Science and Technology*. 170 (2019)
453 60–69. <https://doi.org/10.1016/j.compscitech.2018.11.030>.
- 454 [17] M. Kadlec, R. Růžek, P. Bělský, Concurrent use of Z-pins for crack arrest and
455 structural health monitoring in adhesive-bonded composite lap joints, *Composites
456 Science and Technology*. 188 (2020) 107967.
457 <https://doi.org/10.1016/J.COMPSCITECH.2019.107967>.
- 458 [18] M. Li, Z. Fang, S. Wang, Y. Gu, Y. Li, Z. Zhang, Thermal conductivity
459 enhancement and heat transport mechanism of carbon fiber z-pin graphite
460 composite structures, *Composites Part B: Engineering*. 172 (2019) 603–611.
461 <https://doi.org/10.1016/J.COMPOSITESB.2019.05.092>.

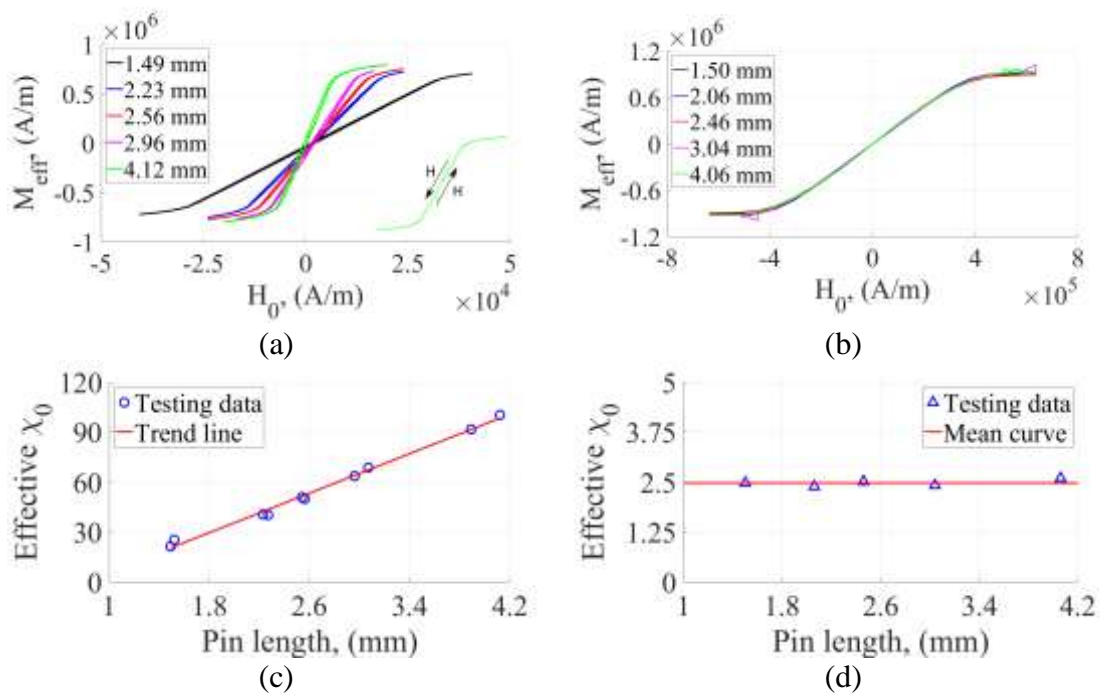
- 462 [19] F. Pegorin, K. Pingkarawat, A.P. Mouritz, Numerical analysis of the heat transfer
463 properties of z-pinned composites, *Composites Communications*. 8 (2018) 14–18.
464 <https://doi.org/10.1016/j.coco.2018.03.002>.
- 465 [20] B. Gu, H. Zhang, B. Wang, S. Zhang, X. Feng, Fracture toughness of laminates
466 reinforced by piezoelectric z-pins, *Theoretical and Applied Fracture Mechanics*. 77
467 (2015) 35–40. <https://doi.org/10.1016/j.tafmec.2015.01.007>.
- 468 [21] J. Summerscales, *Microstructural Characterisation of Fibre-Reinforced*
469 *Composites*, Woodhead Publishing, 1998.
- 470 [22] J.M. Yon, P.H. Mellor, R. Wrobel, J.D. Booker, S.G. Burrow, Analysis of
471 semipermeable containment sleeve technology for high-speed permanent magnet
472 machines, *IEEE Transactions on Energy Conversion*. 27 (2012) 646–653.
473 <https://doi.org/10.1109/TEC.2012.2202232>.
- 474 [23] L.E. Edwards, J.M. Yon, I.P. Bond, P.H. Mellor, Structural magnetic composites
475 for use in electro-mechanical applications, *ICCM International Conferences on*
476 *Composite Materials*. 2015-July (2015) 19–24.
- 477 [24] J. Etches, I. Bond, P. Mellor, Manufacture and applications of magnetically active
478 fibre reinforced composites, *Smart Mater. Struct.* 15 (2006) 288–294.
479 <https://doi.org/10.1088/0964-1726/15/2/007>.
- 480 [25] Prepreg Data Sheet | Hexcel, (2020). <https://www.hexcel.com>.
- 481 [26] Magnetic Property Measurement System, MPMS 3 User’s Manual, (2016).
- 482 [27] M. Schmelz, R. Stolz, Superconducting Quantum Interference Device (SQUID)
483 Magnetometers, in: A. Grosz, M.J. Haji-Sheikh, S.C. Mukhopadhyay (Eds.), *High*
484 *Sensitivity Magnetometers*, Springer International Publishing, Cham, 2017: pp.
485 279–311. https://doi.org/10.1007/978-3-319-34070-8_10.
- 486 [28] S. Hwang, S.-K. Lee, Efficient Experimental Design for Measuring Magnetic
487 Susceptibility of Arbitrarily Shaped Materials by MRI, *Investigative Magnetic*
488 *Resonance Imaging*. 22 (2018) 141–149.
489 <https://doi.org/10.13104/imri.2018.22.3.141>.
- 490 [29] J. Heremans, C.H. Olk, D.T. Morelli, Magnetic susceptibility of carbon structures,
491 *Phys. Rev. B*. 49 (1994) 15122–15125.
492 <https://doi.org/10.1103/PhysRevB.49.15122>.
- 493 [30] D. Jiles, *Introduction to Magnetism and Magnetic Materials*, CRC Press, 2015.
- 494 [31] D.-X. Chen, J.A. Brug, R.B. Goldfarb, Demagnetizing factors for cylinders, *IEEE*
495 *Transactions on Magnetics*. 27 (1991) 3601–3619.
496 <https://doi.org/10.1109/20.102932>.
- 497 [32] D.-X. Chen, E. Pardo, A. Sanchez, Fluxmetric and magnetometric demagnetizing
498 factors for cylinders, *Journal of Magnetism and Magnetic Materials*. 306 (2006)
499 135–146. <https://doi.org/10.1016/j.jmmm.2006.02.235>.
- 500 [33] X.B. Xu, L. Zeng, Ferromagnetic cylinders in earth’s magnetic field—a two-
501 dimensional model of magnetizaion of submarine, (1998) 17.
- 502 [34] M. Sato, Y. Ishii, Simple and approximate expressions of demagnetizing factors of
503 uniformly magnetized rectangular rod and cylinder, *Journal of Applied Physics*. 66
504 (1989) 983–985. <https://doi.org/10.1063/1.343481>.
- 505 [35] M. Yasae, J.K. Lander, G. Allegri, S.R. Hallett, Experimental characterisation of
506 mixed mode traction–displacement relationships for a single carbon composite Z-
507 pin, *Composites Science and Technology*. 94 (2014) 123–131.
508 <https://doi.org/10.1016/j.compscitech.2014.02.001>.

- 509 [36] A. Galehdar, K.J. Nicholson, P.J. Callus, W.S.T. Rowe, S. John, C.H. Wang, K.
510 Ghorbani, The strong diamagnetic behaviour of unidirectional carbon fiber
511 reinforced polymer laminates, *Journal of Applied Physics*. 112 (2012) 113921.
512 <https://doi.org/10.1063/1.4764041>.
- 513 [37] R. Prozorov, V.G. Kogan, Effective Demagnetizing Factors of Diamagnetic
514 Samples of Various Shapes, *Physical Review Applied*. 10 (2018) 1.
515 <https://doi.org/10.1103/PhysRevApplied.10.014030>.
- 516 [38] Multiphysics Simulations Material Library - Adding Material Properties, (2021).
517 <https://www.comsol.com/material-library>.
- 518 [39] Nickel Steel, MAGWEB. (2021). <https://magweb.us/product/nickel-steel/>.
519

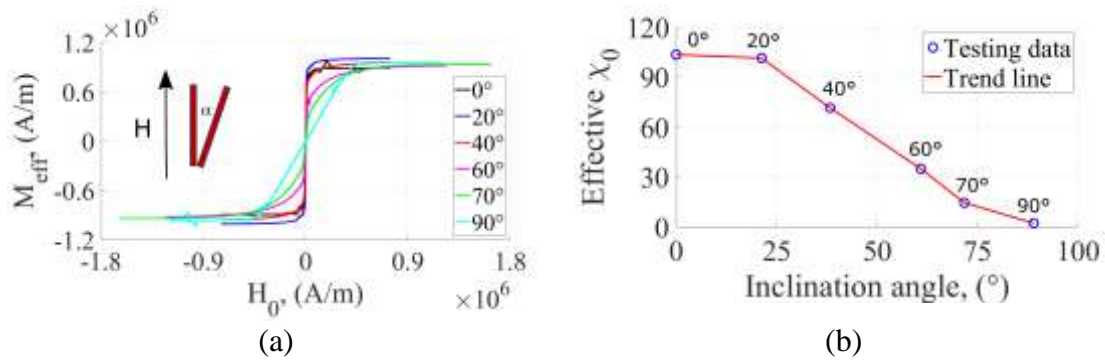
520



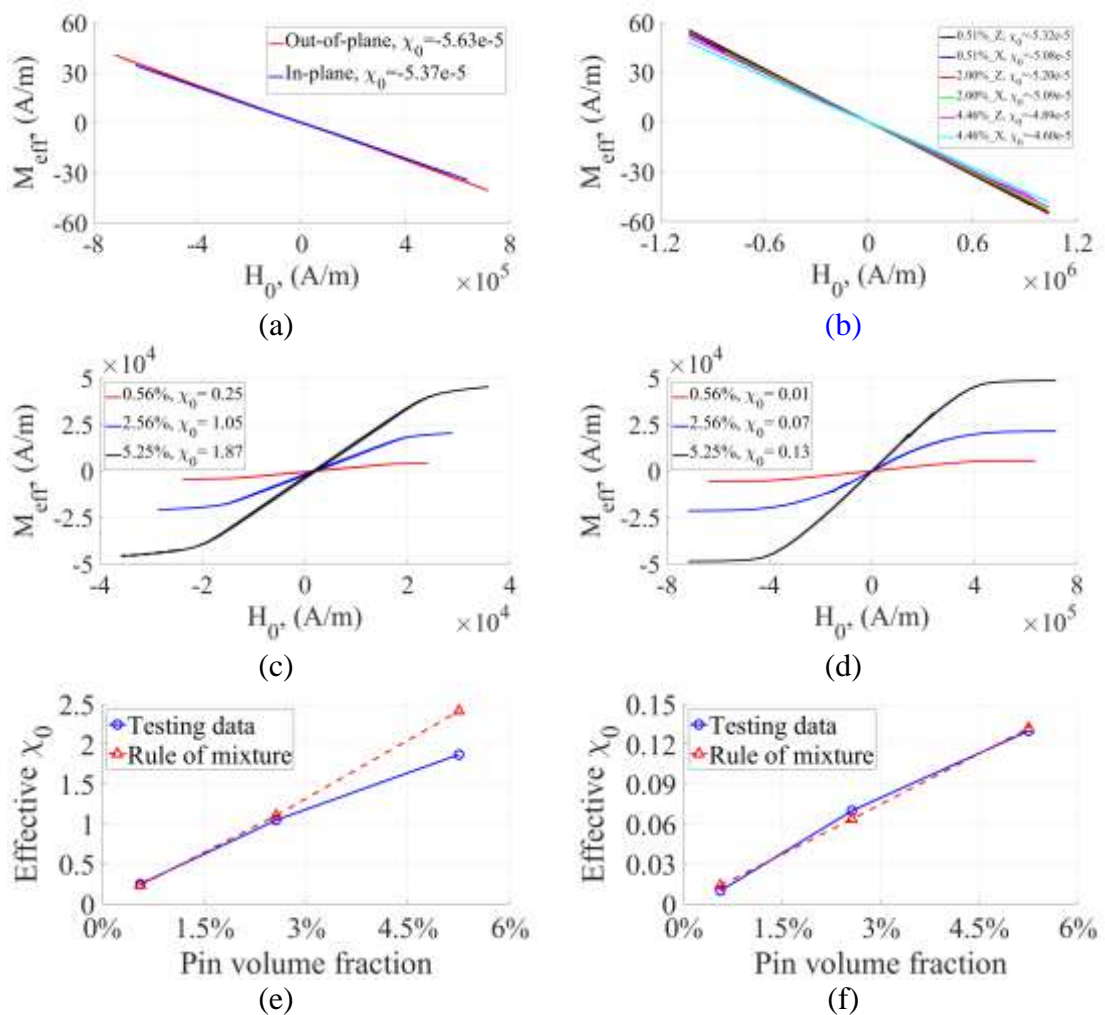
521 Figure 1. (a) Nominal 2% Z-pinned coupon configuration, (b) SQUID MPMS3
 522 and sample installations, (c) schematic of the SQUID detecting system diagram.



523 Figure 2. Ni/Fe pin experimental results: (a) axial M-H curves, (b) radial M-H
 524 curves, (c) axial linear-part effective susceptibility against pin length, (d) radial linear-
 525 part effective susceptibility against pin length.

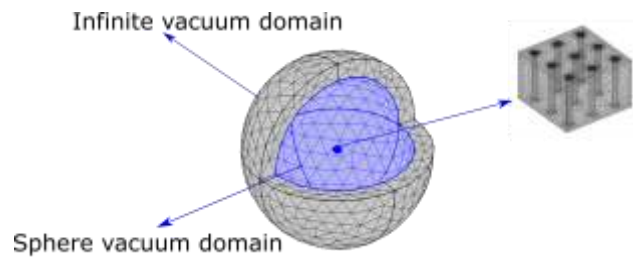


526 Figure 3. Misaligned Ni/Fe pin experimental results: (a) M-H curves, (b) linear-
527 part effective susceptibility against inclination angle.



528 Figure 4. (a) M-H curves of the unpinned sample, (b) M-H curves of carbon FRP
529 Z-pinned samples (out-of-plane: Z, in-plane: X); Ni/Fe Z-pinned samples M-H curves:
530 (c) out-of-plane, (d) in-plane; linear-part effective magnetic susceptibility against the
531 Ni/Fe pin volume fraction: (e) out-of-plane, (f) in-plane

532



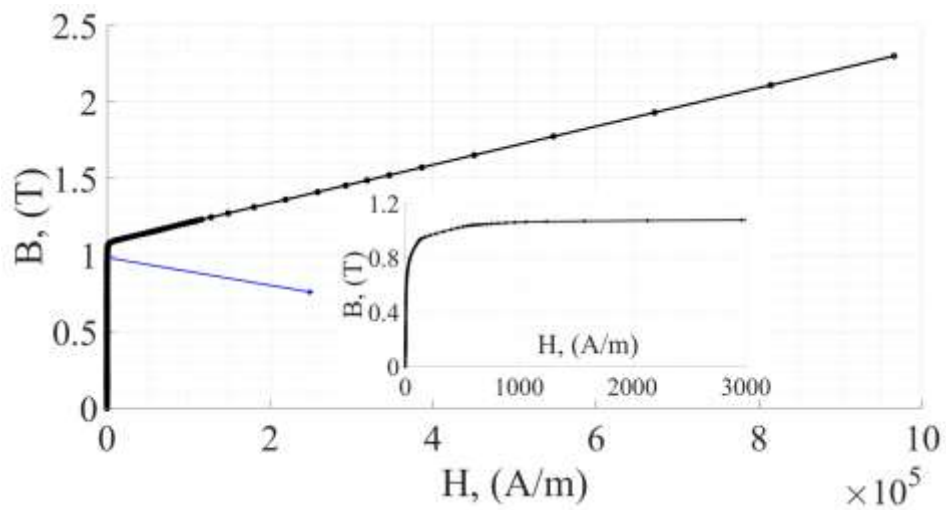
533 Figure 5. FEA model configuration and meshes (A quarter of the model is hidden

534 to make the inner geometry visible).

535

536

537



538

539 Figure 6. Permalloy B-H curve from the COMSOL material library [38,39].

540

541

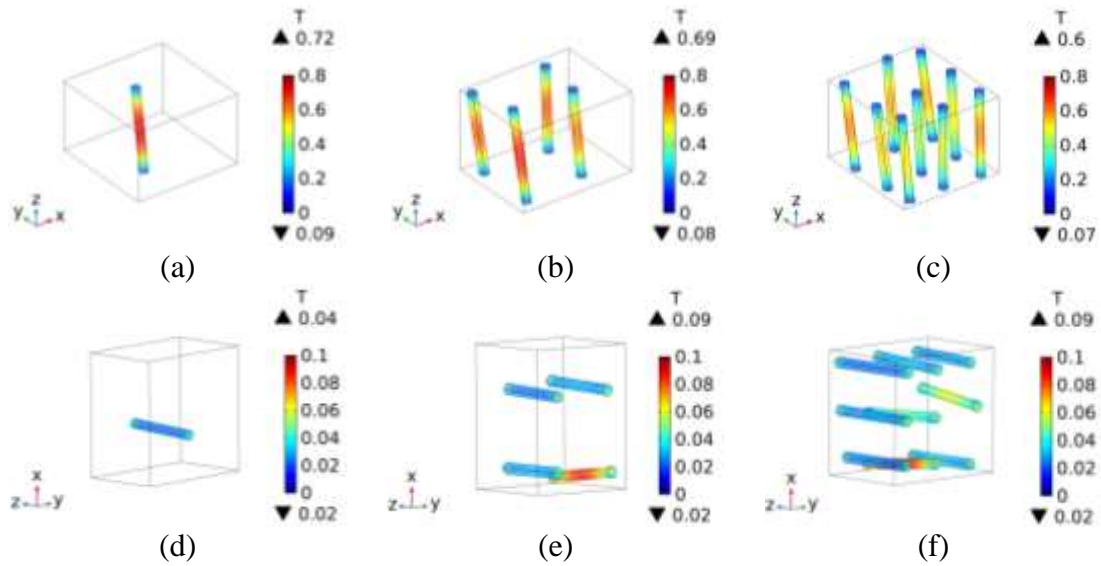
542

543

544

545

546

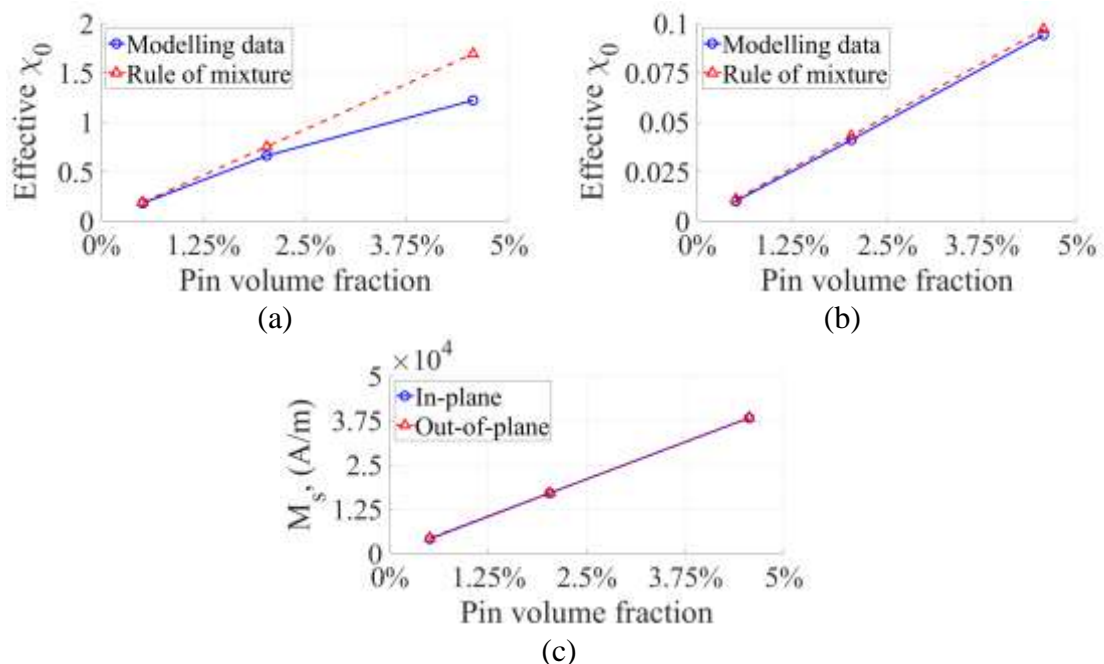


547 Figure 7. Flux density norm of Ni/Fe Z-pinned samples with 10000 A/m magnetic

548 field applied: (a-c) out-of-plane (d-f) in-plane.

549

550

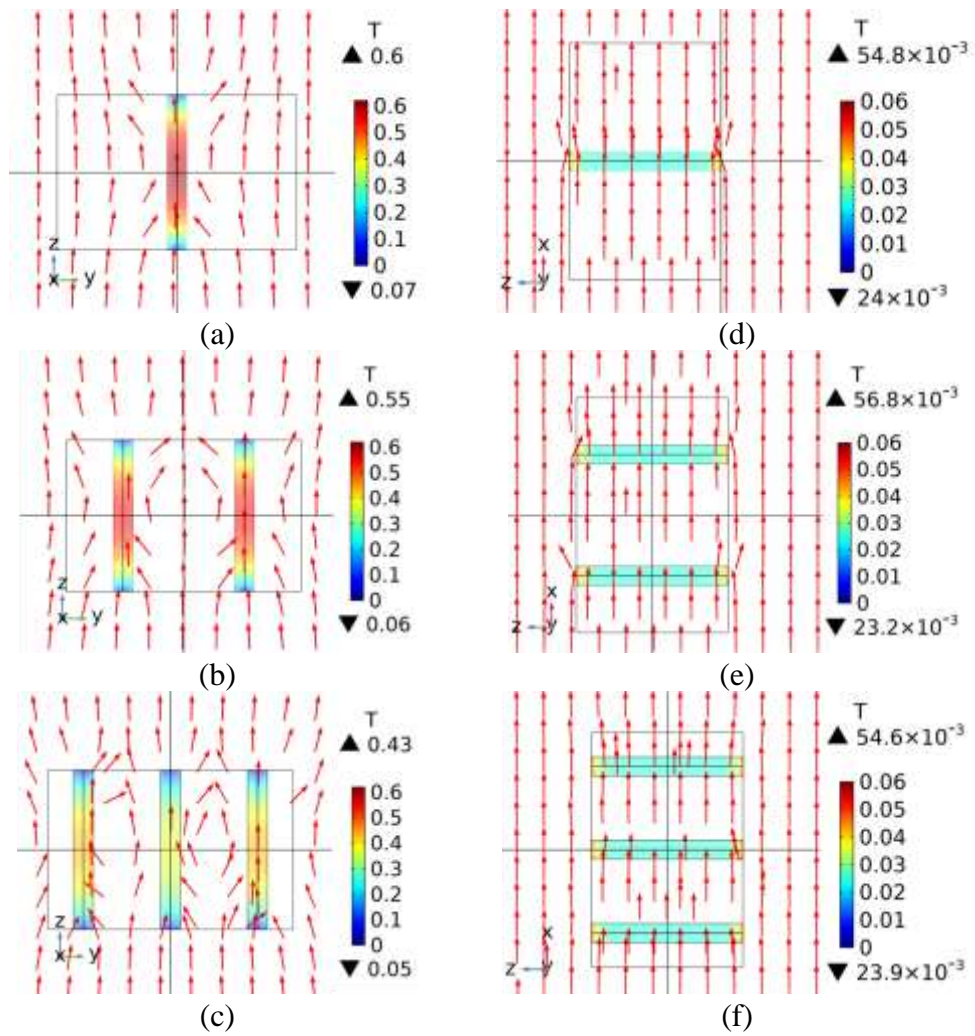


551 Figure 8. Modelling result of ideal Ni/Fe Z-pinned samples: (a) out-of-plane

552 linear-part effective magnetic susceptibility against pin volume fraction, (b) in-plane

553 linear-part effective magnetic susceptibility against pin volume fraction, (c) saturation

554 magnetisation against pin volume fraction.



555 Figure 9. Cross section flux density norm of pins and distribution around them
 556 (modelling result of three ideal Ni/Fe Z-pinned samples with the 10000 A/m magnetic
 557 field applied): (a-c) out-of-plane (d-f) in-plane.

558

559

560

Supplementary document

Mudan Chen, Bing Zhang, Sven Friedemann, Giuliano Allegri, Stephen R. Hallett

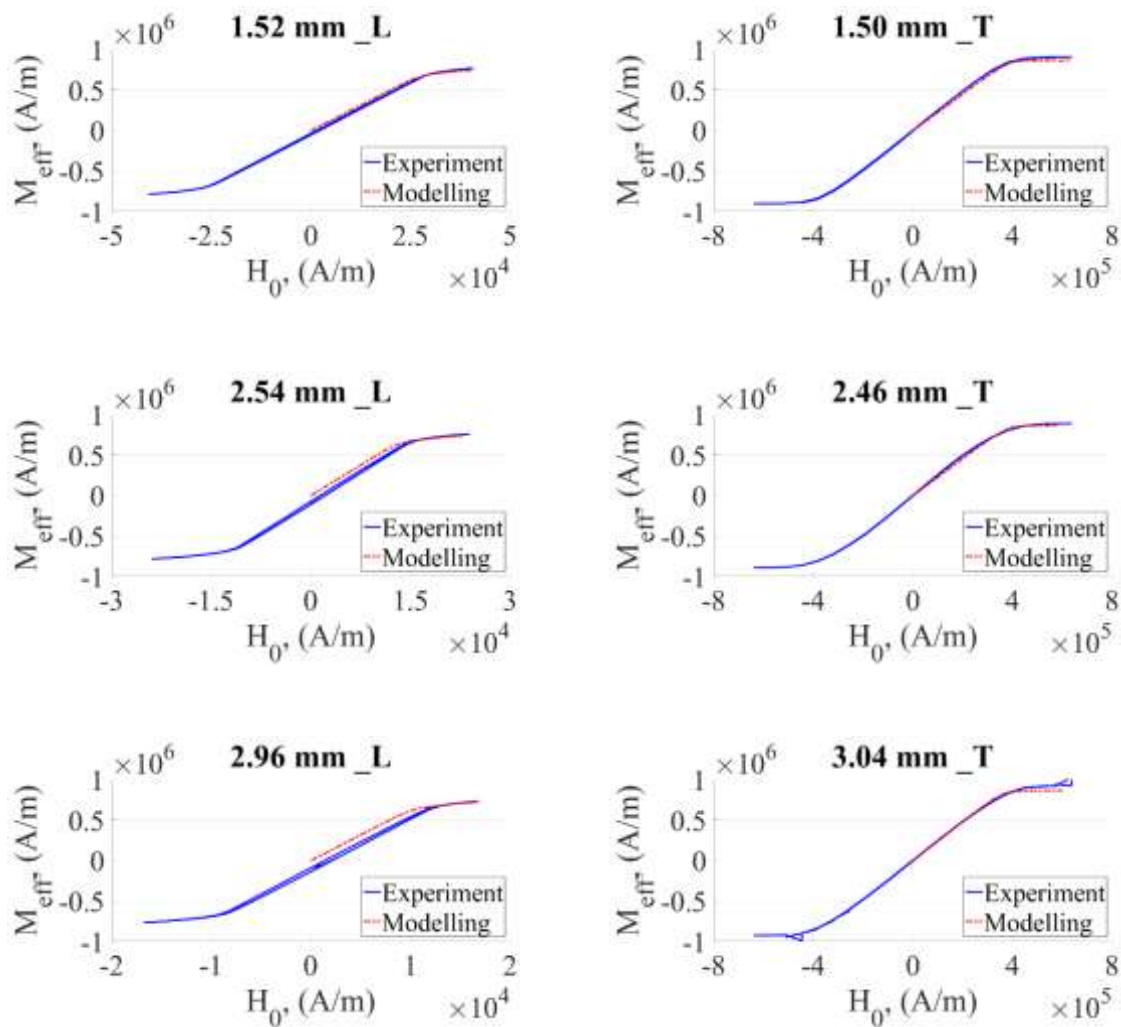


Figure S1. Comparison of experimental and modelling M-H curves of Ni/Fe pins with variable lengths (L: longitudinal, T: radial).

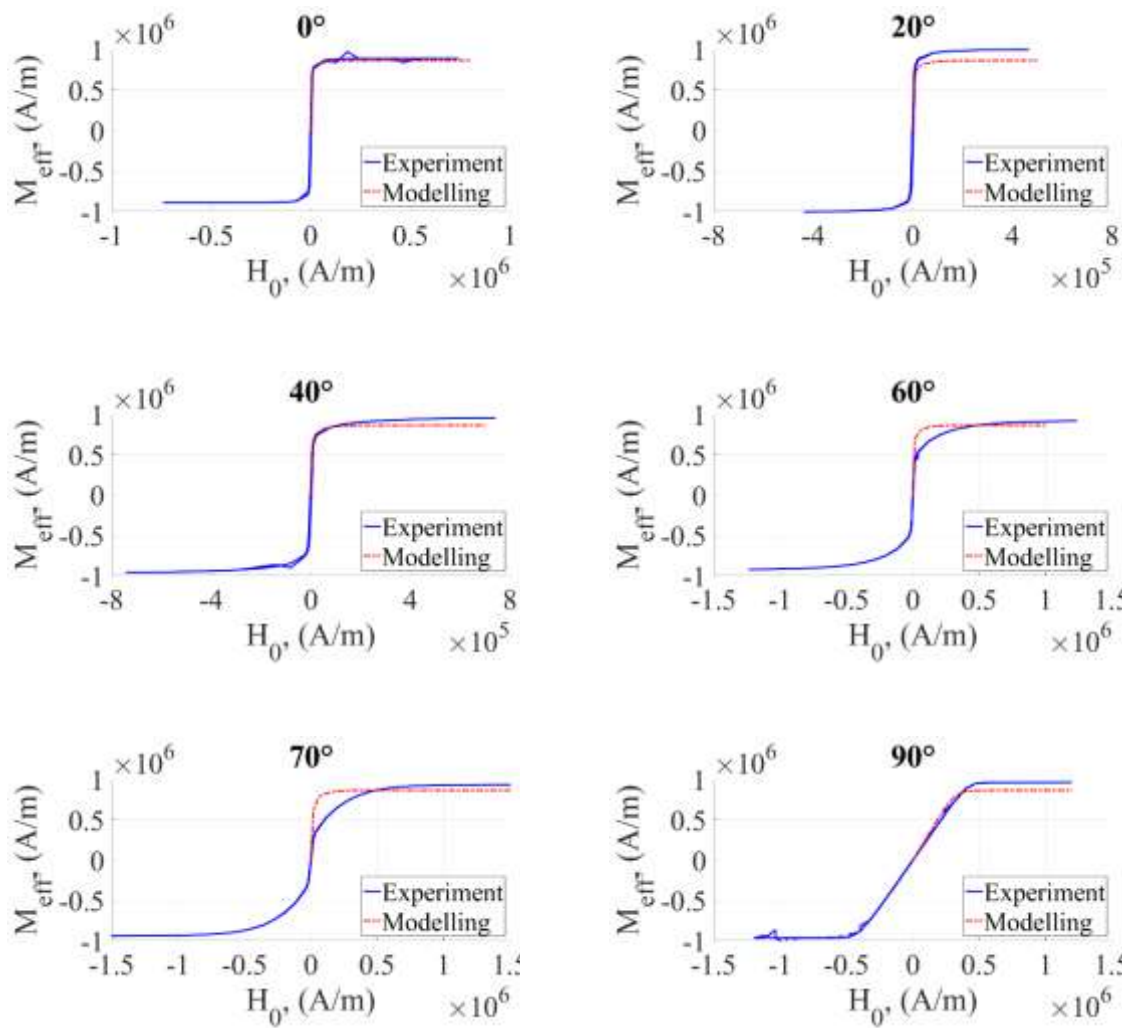


Figure S2. Comparison of experimental and modelling M-H curves of the single 4.05 mm long Ni/Fe alloy pin with variable inclination angles.

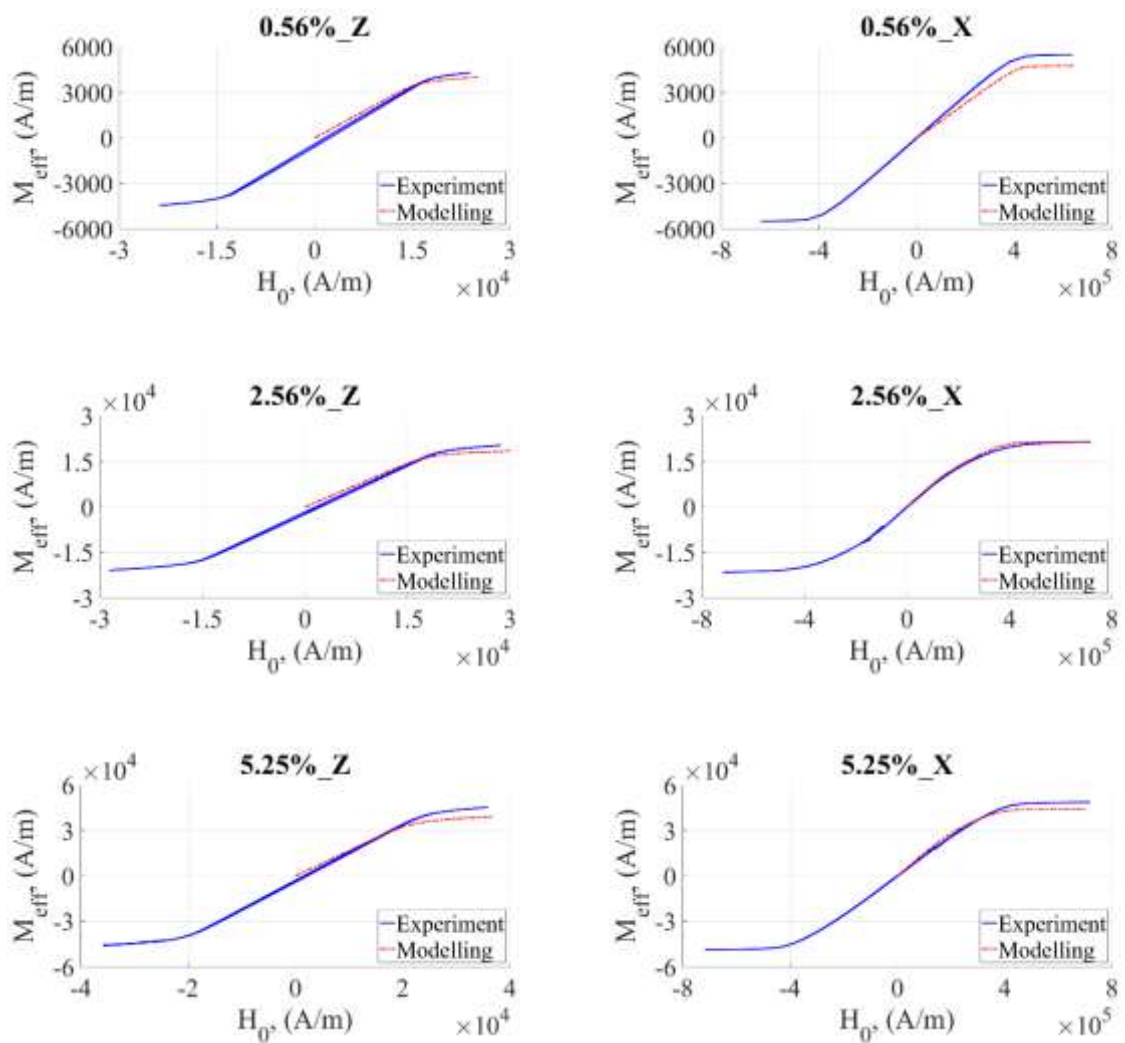


Figure S3. Comparison of experimental and modelling M-H curves of Ni/Fe pins reinforced laminate coupons (Z: out-of-plane, X: in-plane).